Facet controlled anisotropic magnons in Y3Fe5012 thin films

著者	Medwal Rohit, Deka Angshuman, Vas Joseph Vimal, Duchamp Martial, Asada Hironori, Gupta Surbhi, Fukuma Yasuhiro, Rawat Rajdeep Singh
journal or publication title	Applied Physics Letters
volume	119
number	16
page range	162403-1-162403-7
year	2021-10-19
その他のタイトル	Facet controlled anisotropic magnons in Y<inf>3</inf>Fe<inf>5</inf>0<inf>12</inf> thin films
URL	http://hdl.handle.net/10228/00008791

doi: https://doi.org/10.1063/5.0064653

Facet controlled anisotropic magnons in $Y_3Fe_5O_{12}$ thin films

Rohit Medwal[#1], Angshuman Deka[#2†], Joseph Vimal Vas[1], Martial Duchamp[3], Hironori Asada[4], Surbhi Gupta[1,2], Yasuhiro Fukuma[2, 5*], and Rajdeep Singh Rawat[1*]*

[1]Natural Sciences and Science Education, National Institute of Education, Nanyang, Technological University, Singapore 637616 Singapore

[2]Department of Physics and Information Technology, Kyushu Institute of Technology, Iizuka 820-8502, Japan

[3]Laboratory of In-situ and Operando Electron Nanoscopy (LISION), School of Material Science and Engineering, Nanyang Technological University, Singapore 637616 Singapore

[4]Graduate School of Sciences and Technology for Innovation, Yamaguchi University, Ube 755-8611, Japan

[5]Research Center for Neuromorphic AI hardware, Kyushu Institute of Technology, Kitakyushu 808-0196, Japan

[#]These authors contributed equally

Correspondence* rajdeep.rawat@nie.edu.sg,

Co-correspondence** surbhi.gupta@nie.edu.sg, fukuma@cse.kyutech.ac.jp

[†]*Current affiliation:* Purdue University, School of Electrical and Computer Engineering, Birck Nanotechnology Center, West Lafayette, Indiana 47907, USA.

Keywords: Yttrium iron garnet (YIG), ferromagnetic resonance, epitaxial thin films, magnetic anisotropy, anisotropic linewidth, two magnon scattering.

ABSTRACT

Directional specific control on the generation and propagation of magnons is essential for designing future magnon-based logic and memory devices for low power computing. The epitaxy of the ferromagnetic thin film is expected to facilitate anisotropic linewidths which depends on the crystal cut and the orientation of the thin film. Here, we have shown the growth induced magneto-crystalline anisotropy in 40 nm epitaxial Yttrium Iron Garnet (YIG) thin films which facilitates cubic and uniaxial in-plane anisotropy in the resonance field and linewidth for ferromagnetic resonance measurments. The growth induced cubic and non-cubic anisotropy in epitaxial YIG thin films are explained using the short-range ordering of the Fe^{3+} cation pairs in octahedral and tetrahedral sublattices with respect to the crystal growth directions. This site-preferred directional anisotropy enables anisotropic magnon-magnon interaction and opens a new avenue to precisely control the propagation of magnonic current for spin transfer logics using YIG based magnonic technology.

Conduction-electron spin currents in metals dissipate within the spin-diffusion length, typically less than 100 nanometers, which therefore hinders their practical application in information transfer technologies[1-3]. Long range propagation of spin current is essential to transfer the information without much loss in conventional devices that extend laterally in the micrometer scale[4-6]. The decay of spin current in the metallic ferromagnets is mainly caused by scattering of conduction electrons [7]. Magnonic currents in magnetic insulators, on the other hand, which are a collective motion of spins coupled by magnetostatic and/or exchange interactions, persist for long distances of up to a few millimeters (mm)[4,8]. Thus, the insulating ferromagnets provide a promising route towards the development of magnonic devices, powered by the high potential of beyond-CMOS technology[9-12].

Monocrystalline sub-100 nm thick $Y_3Fe_5O_{12}$ (YIG) films typically exhibit ultralow Gilbert damping of the order ~ 10^{-4} which is further reduced to ~10^{-5} for ~ 1 μm thick relaxed films grown by liquid phase epitaxy technique[10,13-15]. Such a low value of Gilbert damping makes YIG a prevalent choice in the emerging field of magnonics and spin wave-based computation[5-6,14-15]. The ability to control the magnon-magnon interaction, reflected through the probing of the linewidth (dH) of the ferromagnetic resonance spectrum, in magnonic devices is interesting because it can allow us to have a better control over the generation and propagation of spin waves[16-20]. A significant development in this field was the recent observation of anisotropic Gilbert damping in ferromagnetic metals[16,19] that can allow an additional degree of control over various resonance linewidth dependent phenomena like spin waves, auto-oscillations etc. Although, the anisotropic linewidths have been observed earlier in nanometer thick YIG thin films[21-25], the facet dependent anisotropic linewidths variation (or anisotropic magnons) and the underlying magnetization relaxation mechanism remains unexplored. In this letter, we investigate the origin of tuning the dH by controlling the facet dependent epitaxial growth of 40 nm YIG thin film. Inductive ferromagnetic resonance (FMR)

spectroscopy was performed, which clearly shows the fourfold (cubic) anisotropy in the YIG (001) and combined uniaxial with cubic anisotropy in the YIG (011) for both the resonant field and the linewidth dH of the FMR spectra. The YIG (111) thin film exhibits relatively low anisotropy in dH and resonance field H_{res}. The influence of this site-preferred directional anisotropy on 2-magnon scattering provides a new potential for directional propagation of magnonic currents which is much needed for dissipation-less low power majority logics and computing devices.

The 40 nm epitaxial YIG films were grown on different orientations of GGG substates. The detail of the deposition conditions and X-ray diffraction measurements of deposited thin film samples are given in the supplementary information S1 and S2, respectively. To investigate the interface of the YIG (001)/GGG (001), YIG (011)/GGG (011) and YIG (111)/GGG (111), atomically resolved high-angle annular-dark-filed (HAADF) scanning transmission electron microscopy (STEM) was employed, and results are shown in Figure 1. The cross-sectional samples for the STEM measurements were prepared using a Zeiss Crossbeam 540 focus ion beam (FIB) and details are given in supplementary information S3[26]. The HAADF-STEM imaging enables us to directly visualize the interface roughness, interface distortion due to lattice mismatch and lattice symmetry. The darker area in the STEM images, in Figure 1(a)-(c), represent YIG thin films while the brighter area represents the GGG substrate. The thickness of all YIG thin films is ~ 40 nm. Atomically resolved STEM images of YIG (001)/GGG (001), YIG (011)/GGG (011) and YIG (111)/GGG (111) interfaces along $[010], [01\bar{1}]$, and $[11\bar{2}]$ zone axis directions are shown in the Figure 1(d)-(f) respectively. Atomically sharp interfaces are observed with no visible interlayer diffusion between YIG and GGG. The roughness of the YIG/GGG interfaces are of one-unit cell. High resolution HAADF-STEM image of the YIG (001), YIG (011) and YIG (111) with their overlapped atomic model created using YIG crystal structure, highlighting the atom positions of Y and Fe

in the YIG unit cell, are shown in the Figure 1(g)-(i) respectively. Thus, combining atomic models with atomically sharp interfaces further confirm the perfect epitaxial growth of YIG thin film along [001], [011] and [111] on corresponding GGG substrate with smooth surfaces and similar roughness.

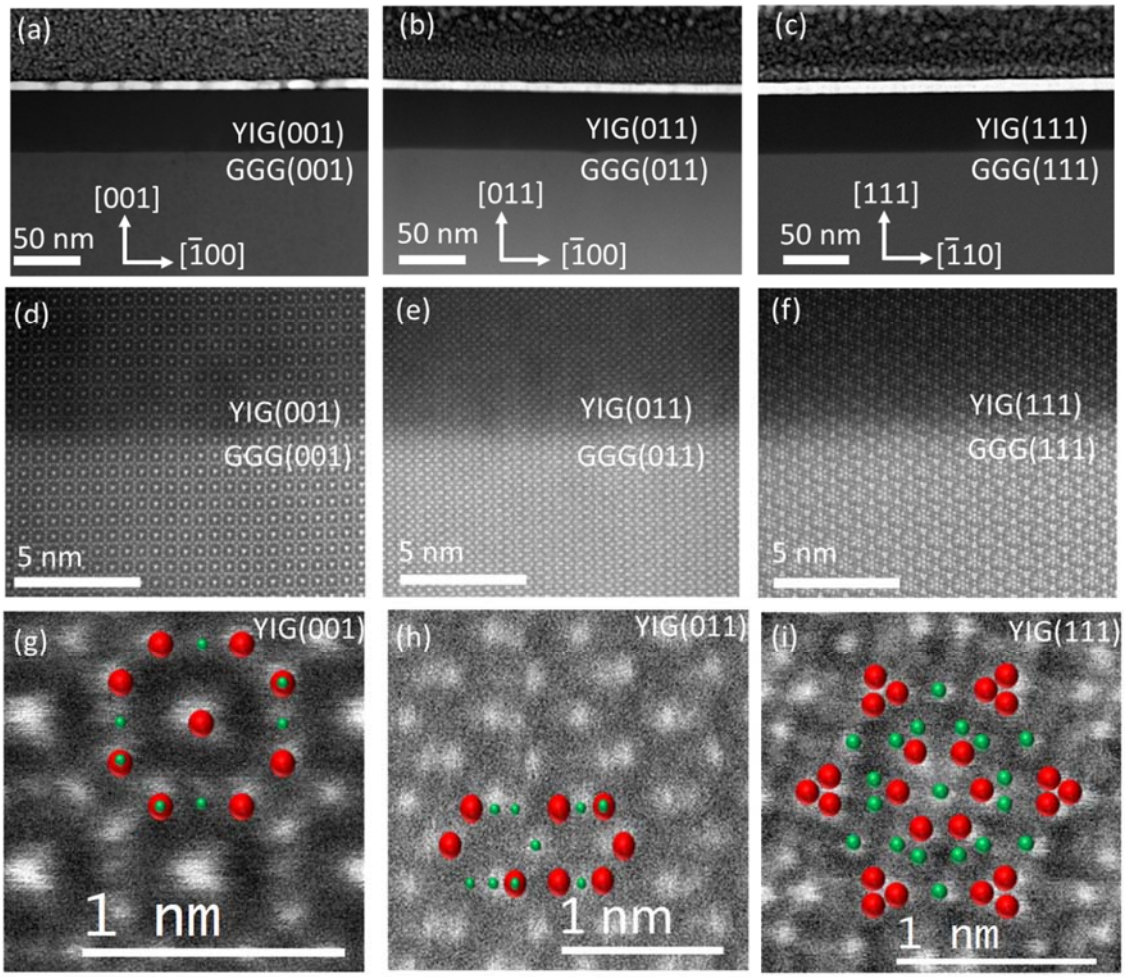

Figure 1. HAADF-STEM images of (a) YIG (001)/GGG (001), (b) YIG (011)/GGG (011) and (c) YIG (111)/GGG (111). High resolution images showing sharp interface (d) YIG (001)/GGG (001), (e) YIG (011)/GGG (011) and (f) YIG (111)/GGG (111). Magnified view showing overlapped atomic model highlighting the Y (red) and Fe (green) atomic positions for (g) YIG (001), (h) YIG (011) and (i) YIG (111).

The deposited thin films were then subjected to flip-chip ferromagnetic resonance (FMR) method for magnetization dynamics studies[27,28]. The measurement schematic with the

orientation of the relevant quantities is given in Figure 2(a). All measurements are performed in static fields well above the in-plane anisotropy fields so that magnetization M of the ferromagnetic layer can be considered parallel to external magnetic field H_{ex}. During magnetization precession, the ferromagnetic system absorbs a part of the applied microwave power thereby giving rise to the recorded FMR spectrum. Typical spectra recorded for the YIG (001), YIG (011) and YIG (111) samples are shown in Figure 2(b). Subsequently the recorded FMR spectra are fitted assuming it to be a sum of symmetric and antisymmetric contributions[29-30]:

$$S11[H] = \frac{L \times dH^2}{(H_{ex} - H_{res})^2 + dH^2} + \frac{D \times dH \times (H_{ex} - H_{res})}{(H_{ex} - H_0)^2 + dH^2}, \qquad (1)$$

where L and D are the Lorentzian and dispersive weights of the FMR lineshape respectively and H_{res} is the resonance field.

FMR linewidth and magnon excitation are strongly dependent on the excitation power used in the FMR measurements[31]. So, we first performed a power dependent FMR measurement in our samples to understand the difference between FMR in the linear and non-linear regimes in YIG thin films. The power dependent spectra and corresponding H_{res} and dH obtained by fitting the spectra using the Eq. (1) is plotted in Figure 2(c) and (d) respectively. Above an input power P_{in} > 5 dBm, the FMR intensity, H_{res} and dH deviates from a constant value. For P_{in} > 5 dBm, the FMR intensity reduces with an increase in both H_{res} and dH. The amplitude of the FMR spectra depends on the absorbed microwave power which changes the susceptibility χ of the magnetic material. This can be understood from the equation $\frac{\chi''}{\chi_0''} = \frac{M_{res}}{M_s} = \left(1 + \frac{\gamma^2 h_{rf}^2}{2\pi f^2}\right)^{-1}$ [32,33]. Here, γ is the gyromagnetic ratio, h_{rf} is the microwave field. At low excitation powers (i.e. at low h_{rf}), the precession cone angle is small and therefore, M_{res} will be equal to saturation magnetization M_s. This results in a constant amplitude of FMR spectra.

However, as the excitation power is increased above a certain threshold, due to a larger precession cone angle we obtain a decrease in the FMR signal amplitude. This can be quantitatively understood using the $\left(1+\frac{\gamma^2 h_{rf}^2}{2\pi f^2}\right)^{-1}$ dependence, which shows that at high values of h_{rf}, it deviates from a constant behavior[34]. A similar power dependence is also observed for the YIG (001)/GGG (001) and YIG (011)/GGG (011) samples. To eliminate contributions from such non-linear effects, we use an input power P_{in} = 0 dBm to study the magnetization dynamic properties using the FMR spectroscopy.

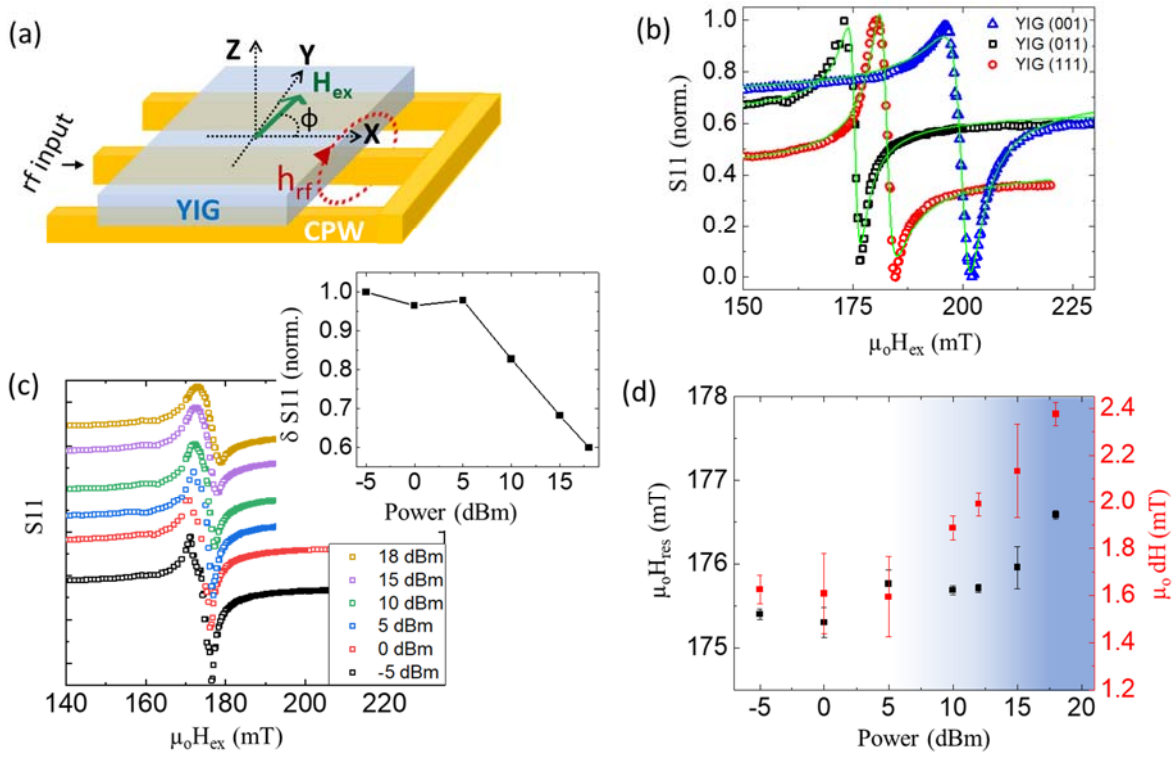

Figure 2. (a) Schematic of the experimental geometry used in the ferromagnetic resonance (FMR) measurements showing the direction of microwave current in coplanar waveguides below the YIG thin film I_{rf}, an illustrative Oersted field h_{rf} and the orientations of magnetization M and in-plane external field H_{ex} with respect to the co-ordinate axes. (b) Typical spectra obtained from the vector network analyzer (VNA) based FMR measurements in the YIG samples at f = 7 GHz and ϕ = 60°, along with fit to Eq. (1). (c) The corresponding input power

dependence of FMR spectra. Inset shows the values of normalized peak to peak amplitudes of S11 spectra. (d) Power dependence of resonance fields H_{res} and FMR linewidths dH. The data shown in (c) and (d) corresponds to YIG (011). Similar behavior is seen for YIG (001) and YIG (111) as shown in the supporing information section S4.

Frequency dependent FMR spectra were recorded for the three orientations of epitaxial YIG thin films and the corresponding H_{res} obtained are plotted in Figure 3(a). The monotonous increase with frequency f that agrees well with the Kittel formula $f = \frac{\gamma}{2\pi}\sqrt{H_{res}(H_{res} + 4\pi M_{eff})}$ confirms the excitation of FMR[35]. The values of effective magnetization M_{eff} obtained from fitting the H_{res} vs f for each sample, keeping $\frac{\gamma}{2\pi} = 28.5$ GHz/mT , is presented in the inset. However, the difference in M_{eff} with values of the saturation magnetization of 175 mT indicates the presence of magnetic anisotropy fields in the YIG thin films. The obtained values of dH are plotted in Figure 3(b). A linear increase in the linewidth is observed up to 10 GHz. Thereafter, this linear dependency is suppressed for higher frequencies above 10 GHz for all our epitaxial thin films. Such a frequency dependence indicates the presence of 2-magnon scattering in the magnetization relaxation processes[36]. Additionally, in the same figure, we observe a strong dependence of the dH on the epitaxy of the thin films despite being deposited simultaneously under similar conditions on the three different substrates. This indicates that the epitaxy of the thin film plays a role not only on the magnetic anisotropy fields, but also on the dynamical magnetization relaxation processes.

We performed an angular dependent FMR measurement to understand the facet dependent magnetic anisotropy and its effect on the magnetic damping. The magnetic anisotropy of the cubic YIG crystal is given by $E_a = K_1(\alpha_1^2\alpha_2^2 + \alpha_2^2\alpha_3^2 + \alpha_3^2\alpha_1^2) + K_2\alpha_1^2\alpha_2^2\alpha_3^2$. The K_1 and K_2 are the first and second order magneto-crystalline anisotropies of the cubic system and α_1, α_2, and α_3 are direction cosines with respect to the magnetization vector. The

observed resonant field at f = 7 GHz is plotted as a function of ϕ in the 2D contour color maps shown in Figure 3(c)-(e). Three distinct behaviors are observed. In case of the YIG (001), we observed a dominant four-fold angular dependence which is well matched with the first order anisotropy field given by $E_a = \frac{K_1}{8}(1 - \cos 4\phi)$ for the YIG grown along (001). The angular dependence for YIG grown along (011) shows a dominant two-fold symmetry along with the tiny four-fold symmetry. The observed combination of the two-fold and four-fold symmetry in the YIG (011) is in accordance with $E_a = \frac{K_1}{32}(7 - 4\cos 2\phi - 3\cos 4\phi)$. On the other hand, the FMR spectra of YIG grown in (111) direction shows almost angle independent behavior. The first order anisotropy for (111) facet is calculated to be independent of the angular rotation of magnetization which is equal to $K_1/4$. Such a ϕ dependence indicates the presence of growth direction dependent uniaxial $H_{2\|}$ and cubic $H_{4\|}$ in-plane anisotropy fields.

This growth induced magneto-crystalline anisotropy (MCA) can be explained using the framework of short-range ordering of the Fe^{3+} cation pairs in the garnet film during the crystalline growth. Two types of relevant rare earth Fe^{3+} pair ordering- tetrahedral and octahedral, are present in the films, which arises from the bonding between Fe^{3+} and O^{2-}. The arrangement of the tetrahedral and octahedral sublattices in the YIG lattice are given in the supplementary section S5. The ordering of both tetrahedral and octahedral sublattices in YIG (001) show a cubic symmetry. However, for YIG (011), tetrahedral and octahedral ordering shows a cubic and uniaxial symmetry, respectively. Based on this, we can conclude that the tetrahedral and octahedral Fe^{3+} sublattices have a dominant contribution to cubic and uniaxial MCA respectively.

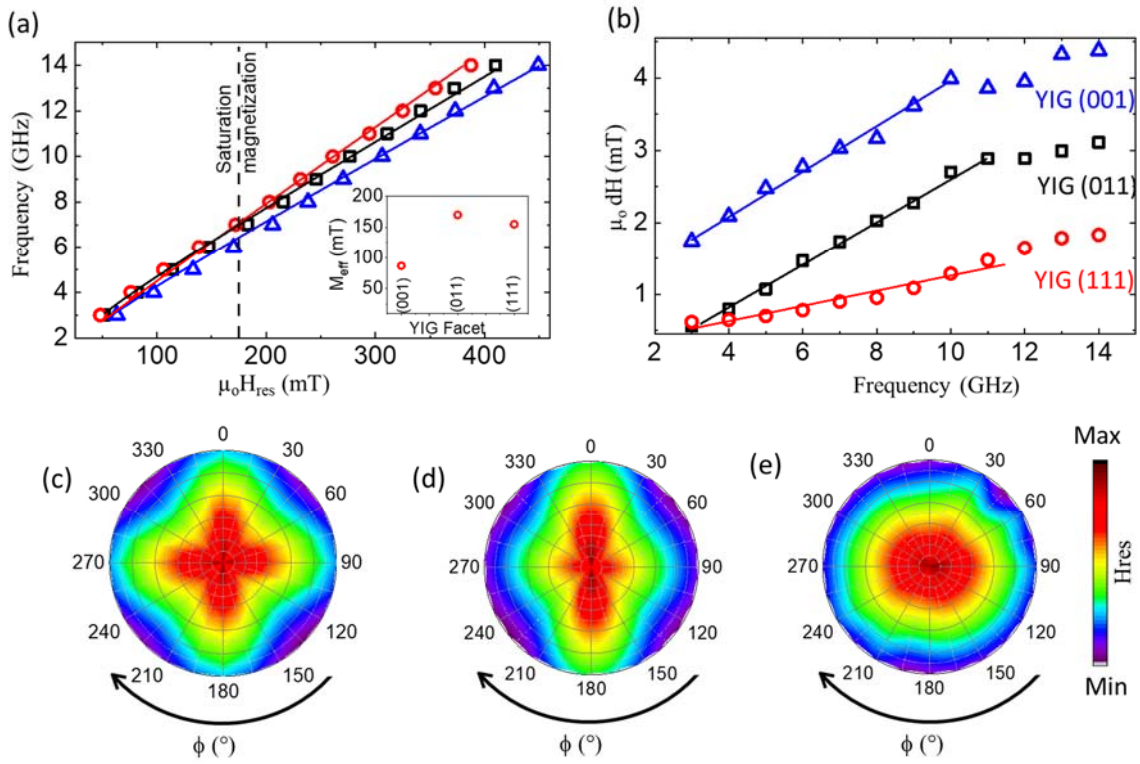

Figure 3. (a) Resonance fields as a function of frequency for the three YIG samples along with Kittel fits at ϕ = 60 degree. Broken vertical line at 170 mT shows the saturation magnetization of the YIG. Inset shows the values of effective magnetization M_{eff} obtained for YIG (001), YIG (011) and YIG (111). (b) Frequency dependence of linewidths dH at ϕ = 60 degree. 2D contour color maps ((c)-(e)) of magnitude of resonance field as a function of ϕ for YIG (001), YIG (011) and YIG (111) obtained from S11 spectra.

An in-plane angular dependence of H_{res} at a fixed frequency enables us to quantify in-plane anisotropy fields with greater accuracy compared to that obtained from the Kittel fit of the H_{res} vs f dependence because $H_{2\parallel}$ and $H_{4\parallel}$ are typically about 1-2 orders smaller than the demagnetizing field[18]. The resonance fields at f = 7 GHz as a function of ϕ for the three samples are shown in Figure 4(a)-(c). To obtain the anisotropy fields in YIG (001), YIG (011) and YIG (111), the ϕ dependence of H_{res} is fitted using [23]:

$$\left(\frac{\omega}{\gamma}\right)^2 = \left\{H + H_{4\parallel}\cos 4\phi - H_{2\parallel}\cos\left(2\phi - \frac{\pi}{2}\right)\right\}\left\{H + 4\pi Meff + \frac{H_{4\parallel}(3+\cos 4\phi)}{4} + H_{2\parallel}\sin^2\left(\phi - \frac{\pi}{4}\right)\right\} \quad (2)$$

The values of $\mu_0 H_{4\parallel}$ are ~ -4.5 mT for YIG (001), ~ 4.1 mT for YIG (011) and ~ 0.08 mT for YIG (111), while the value of $\mu_0 H_{2\parallel}$ are ~0.9 mT for YIG (001), ~ -9.0 mT for YIG (011) and ~ -0.7 mT for YIG (111). The linewidths of the FMR spectra are plotted as a function of ϕ for the respective samples in Figure 4(d)-(f). A striking resemblance in the periodicity of the linewidths and the resonance fields are observed. This indicates that MCA, which arises from the epitaxial nature of the thin films, plays a role in the resonance linewidths. The phase difference between periodicity of H_{res} and dH is found to be 180°. In the following section we explain the anisotropic linewidths as arising from an epitaxy dependent 2-magnon scattering process in our samples.

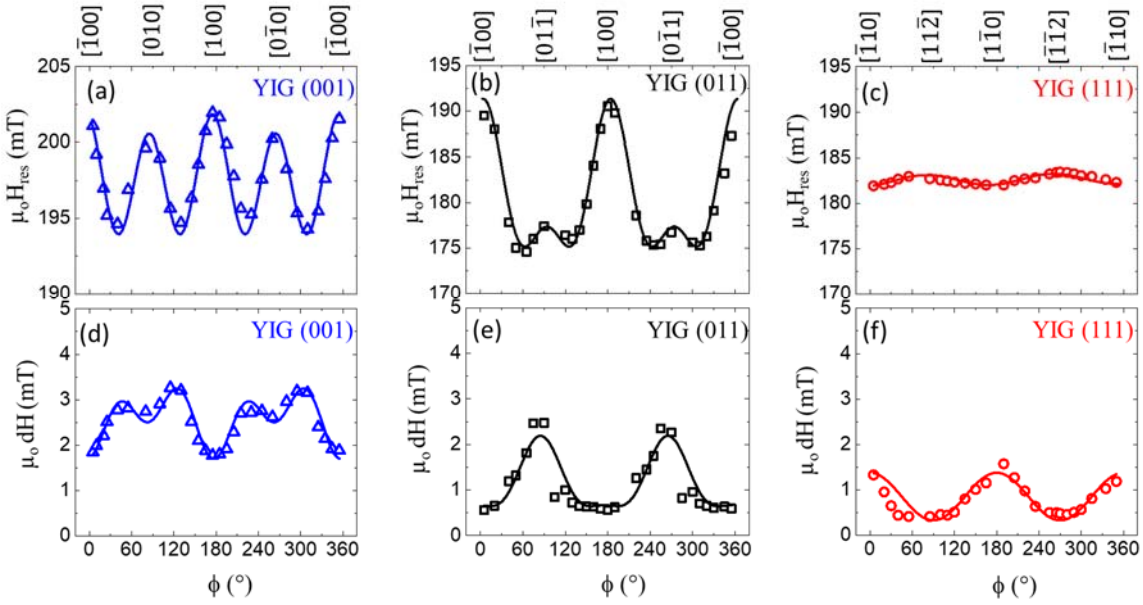

Figure 4. FMR resonant field as a function of ϕ obtained by fitting the S11 spectra at f = 7 GHz for (a) YIG (001), (b) YIG (011) and (c) YIG (111). The solid lines shown in (a)-(c) are the fitting of resonant field as a function of ϕ, using the Eq. (2). The corresponding values of resonance linewidths dH are plotted in (d)-(f) respectively. The solid lines shown in (d)-(f) are fitting using Eq. (3). The anisotropy values obtained from the fitting are given in Table 1.

FMR linewidths can be expressed as the sum of contributions from inhomogeneous broadening, Gilbert damping, mosaicity and the 2-magnon scattering: $dH = dH_0 + dH_{mosaic} + dH_{Gilbert} + dH_{2-magnon}$ [36,37]. The effect of field-dragging i.e., the case where M is not parallel to the H_{ex} can be ignored because the applied magnetic fields during resonance are well above the MCA in the in-plane magnetized films. The effect of inhomogeneous broadening on the anisotropic linewidth behavior can be ignored because it is independent of ϕ [30]. The mosaicity effect on linewidths which arises due to the non-uniformity of the sample parameters such as thickness and internal magnetic energies, is zero along the easy in-plane direction[30]. A relatively higher value of resonance linewidths compared to completely relaxed thin films indicates the presence of extrinsic contributions from 2-magnon scattering, as has also been observed from the frequency dependent linewidths. The 2-magnon process arises from the scattering of resonant modes with $k = 0$ into non-uniform $k \neq 0$ magnon modes at thin film interfaces. Such a magnon wavevector k lies in the film plane and the strength of the scattering process increases as the angle between magnetization vector and k decreases below the critical angle $\xi = \sin^{-1}\left(\frac{H_{res}}{H_{res}+4\pi M_{eff}}\right)^{0.5}$ [38]. For our YIG films, we can estimate the value of $\xi \sim 50$ degree. Since the measurements are performed for in-plane magnetized films ($\phi = 0$ degree), the 2-magnon contribution is expected to be maximized. We fitted the in-plane ϕ dependent linewidths of our samples with the ϕ dependence of 2-magnon scattering process using the equation[37-41]:

$$dH = dH_{sum} + \left[A + B\cos 2\left(\phi - \phi_{uni}\right) + C\cos 4\left(\phi - \phi_{cub}\right)\right]\sin^{-1}\left(\frac{f}{\sqrt{f^2+f_0^2}+f_0}\right) \qquad (3)$$

where, the dH_{sum} is the sum of angular independent inhomogeneous broadening, Gilbert damping and mosaicity contributions. The second term corresponds to 2-magnon scattering which has been written as the sum of three terms with A and C being contributions from the

four-fold cubic anisotropy and B being contribution from a two-fold uniaxial anisotropy. The obtained values from the fitting of the linewidths using Eq. (3) is given in Table 1. In case of the YIG (111), where $\mu_0 H_2 = 0.7$ mT and $\mu_0 H_{4\|} = 0$ mT, we can fit the data using only the term that has twofold uniaxial symmetry. For the YIG (001) and YIG (011) samples, we need to factor in contributions from all the three terms i.e., angle independent (A), two-fold (B) and four-fold (C) terms. A and C which correspond to contributions from a fourfold symmetry increases with increasing H_4 and are highest for YIG (001). On the other hand, B is maximum for YIG (011), which has the highest value of H_2. Our results clearly demonstrate the facet dependent anisotropic linewidth in the YIG thin film. Such an observation indicates that the YIG/GGG interface dislocations could be dependent on the corresponding epitaxy and therefore gives rise to an anisotropic 2-magnon scattering process which is dependent on the facet.

Table 1. Summary of values obtained from fitting using Eq. (2) and (3) for FMR measurements at $f = 7$ GHz.

YIG facet	$\mu_0 H_{2\|}$ (mT)	$\mu_0 H_{4\|}$ (mT)	A (mT)	B (mT)	C (mT)
(001)	0.9	-4.5	110	55	40
(011)	-9.0	4.1	75	80	25
(111)	-0.7	0.08	0	50	0

In conclusion, we have demonstrated and explained the origin of facet dependent anisotropic magnon-magnon interaction reflected in ferromagnetic resonance linewidths - a fundamental parameter for the magnetization relaxation process. The highly epitaxial thin films of YIG (001), YIG (011) and YIG (111) with atomically sharp interfaces was successfully grown and confirmed using X-ray diffraction and scanning transmission electron microscopy studies. The YIG (001) thin films clearly reveal four-fold anisotropic linewidth whereas the YIG (011) thin films show a dominant two-fold symmetry along with the tiny four-fold symmetry. The observed facet dependent anisotropic resonance linewidth will enrich the

understanding of the magnetization relaxation mechanism in the YIG thin films much required for the spin transport in the epitaxial YIG thin films interfacing with heavy metals[42,43]. This will also enable direction specific generation, propagation and relaxation of magnonic current and will push forward the YIG as an important material, for power efficient magnon-based logic and memory applications[41-47]. Therefore, our demonstration of epitaxy dependent anisotropic linewidths is very important for nanoscale magnetism and provide a route towards to design YIG based low loss spintronics devices in future.

ACKNOWLEDGEMENT

This work was supported by the Ministry of Education (MOE) through grant numbers MOE2017-T2-2-129, MOE2019T2-1-058 and NRF-CRP21-2018-003. Y.F. acknowledges the Japan Society for the Promotion of Science for supporting this work through grant no. 18H01862. M.D. acknowledges the financial support from Nanyang Technological University start-up grant M4081924 and MOE tier 1 through grant 2019-T1-001-066. Transmission electron microscopy imaging were performed at the Facility for Analysis, Characterization, Testing and Simulation (FACTS) in Nanyang Technological University, Singapore.

DATA AVAILABILITY

The data that support the findings of this study are available from the corresponding author upon reasonable request.

REFERENCES

1. J. Bass, and W.P. Pratt Jr, Spin-diffusion lengths in metals and alloys, and spin-flipping at metal/metal interfaces: an experimentalist's critical review. *J. Phys.: Condens. Matter* **19**, 183201 (2007).
2. K. Roy, Estimating the spin diffusion length and the spin Hall angle from spin pumping induced inverse spin Hall voltages. *Phys. Rev. B* **96**, 174432 (2017).
3. U. Shashank, R. Medwal, T. Shibata, R. Nongjai, J. V. Vas, M. Duchamp, K.Asokan, R. S. Rawat, H. Asada, S. Gupta, and Y. Fukuma, Adv. Quantum Technol. 4, 2000112 (2021).
4. L.J. Cornelissen, J. Liu, R.A. Duine, J.B. Youssef, and B.J. van Wees, Long-distance transport of magnon spin information in a magnetic insulator at room temperature. *Nat. Phys.* **11**, 1022-1026 (2015).
5. H. Qin, G.J. Both, S.J. Hamalainen, L. Yao, and S. van Dijken, Low-loss YIG-based magnonic crystals with large tunable bandgaps. *Nat. Commun.* **9**, 5445 (2018).
6. C. Liu et al., Long-distance propagation of short-wavelength spin waves. *Nat. Commun.* **9**, 738 (2018).
7. V. Zayets, Spin and charge transport in materials with spin-dependent conductivity. *Phys. Rev. B* **86**, 174415 (2012).
8. H. Qin, S.J. Hämäläinen, K. Arjas, J. Witteveen, and S. van Dijken, Propagating spin waves in nanometer-thick yttrium iron garnet films: Dependence on wave vector, magnetic field strength, and angle. *Phys. Rev. B* **98**, 224422 (2018).
9. J. Mendil et al., Magnetic properties and domain structure of ultrathin yttrium iron garnet/Pt bilayers. *Phys. Rev. Mater.* **3**, 034403 (2019).
10. L. Soumah et al., Ultra-low damping insulating magnetic thin films get perpendicular. *Nat. Commun.* **9**, 3355 (2018).
11. Q.B. Liu et al., Unusual anomalous Hall effect in perpendicularly magnetized YIG films with a small Gilbert damping constant. *Phys. Rev. B* **101**, 174431 (2020).
12. Y. Zhou et al., Current-Induced In-Plane Magnetization Switching in a Biaxial Ferrimagnetic Insulator. *Phys. Rev. Appl.* **13**, 064051 (2020).
13. R. Medwal et al., Magnetoimpedance of Epitaxial $Y_3Fe_5O_{12}$ (001) Thin Film in Low-Frequency Regime. *ACS Appl Mater Interfaces* **12**, 41802 (2020).
14. Y. Kajiwara et al., Transmission of electrical signals by spin-wave interconversion in a magnetic insulator. *Nature* **464**, 262 (2010).
15. B. Heinz et al., Propagation of Spin-Wave Packets in Individual Nanosized Yttrium Iron Garnet Magnonic Conduits. *Nano Letters* **20**, 4220 (2020).
16. Y. Li et al., Giant Anisotropy of Gilbert Damping in Epitaxial CoFe Films. *Phys. Rev. Lett.* **122**, 117203 (2019).
17. A. Deka et al., Electric-field control of interfacial in-plane magnetic anisotropy in CoFeB/MgO junctions. *Phys. Rev. B* **101**, 174405 (2020).
18. H. Kurebayashi et al., Uniaxial anisotropy of two-magnon scattering in an ultrathin epitaxial Fe layer on GaAs. *Appl. Phys. Lett.* **102**, 062415 (2013).
19. L. Chen et al., Emergence of anisotropic Gilbert damping in ultrathin Fe layers on GaAs(001). *Nat. Phys.* **14**, 490 (2018).
20. Z. Chen et al., The anisotropic effective damping of thickness-dependent epitaxial Co2FeAl films studied by spin rectification. *Appl. Phys. Lett.* **112**, 122406 (2018).
21. C. Vittoria, H. Lessoff, and N. Wilsey, Induced in-plane magnetic anisotropy in YIG films. *IEEE Trans. Magn.* **8**, 273 (1972).
22. Y-Q. Wang, and X-Y. Zeng, *Hyperfine Intreactions* **28**, 4 (1986).
23. H. Wang, C. Du, P.C. Hammel, and F. Yang, Strain-tunable magnetocrystalline anisotropy in epitaxial $Y_3Fe_5O_{12}$ thin films. *Phys. Rev. B* **89**, 134404 (2014).

24. S.A. Manuilov, S.I. Khartsev, and A.M. Grishin, Pulsed laser deposited $Y_3Fe_5O_{12}$ films: Nature of magnetic anisotropy I. *J. Appl. Phys.* **106**, 123917 (2009).
25. S.A. Manuilov, and A.M. Grishin, Pulsed laser deposited $Y_3Fe_5O_{12}$ films: Nature of magnetic anisotropy II. *J. Appl. Phys.* **108**, 013902 (2010).
26. E. Tykalova et al., Challenges and Applications to Operando and In Situ TEM Imaging and Spectroscopic Capabilities in a Cryogenic Temperature Range, *Acc. Chem. Res.* **54,** 3125 (2021).
27. R. Medwal, S. Gupta, R. S. Rawat, A. Subramanian, Y. Fukuma , Spin Pumping in Asymmetric $Fe_{50}Pt_{50}$/Cu/$Fe_{20}Ni_{80}$ Trilayer Structure, *Physica status solidi (RRL) - Rapid Research Letters* **13**, 1900267 (2019).
28. S. Gupta, D. Kumar, T. L. Jin, R. Nongjai, K. Asokan, A. Ghosh, M. Aparnadevi, P. Suri, and S. N. Piramanayagam, *AIP Advances* **8**, 056125 (2018)
29. U. Shashank et al., Highly dose dependent damping-like spin–orbit torque efficiency in O-implanted Pt, *Appl. Phys. Lett.* **118**, 252406 (2021)
30. J. V. Vas, R. Medwal, U. Chaudhuri, M. Mishra, A. Chaurasiya, R. Mahendiran, S. N. Piramanayagam, R. S. Rawat, C. K. P. Lee, Broad-energy oxygen ion implantation controlled magnetization dynamics in CoFeTaZr, J. Alloys and Compounds **872** 159685 (2021).
31. B. Rana, Y. Fukuma, K. Miura, H. Takahashi, and Y. Otani, Effect of excitation power on voltage induced local magnetization dynamics in an ultrathin CoFeB film. *Sci. Rep.* **7**, 2318 (2017).
32. N. Bloombergen, and S. Wang, Relaxation Effects in Para- and Ferromagnetic Resonance. *Phys. Rev.* **93**, 1 (1954).
33. A.G. Gurevich, and G.A. Melkov, G.A. Magnetization Oscillation and Waves (CRC Press, Inc., 1996).
34. H. Suhl, The theory of ferromagnetic resonance at high signal powers. *Phys. Chem. Sol.* **1**, 209-227 (1957).
35. S. Gupta, R. Medwal, D. Kodama, K. Kondou, Y. Otani, and Yasuhiro Fukuma, Important role of magnetization precession angle measurement in inverse spin Hall effect induced by spin pumping, *Appl. Phys. Lett.* 110, 022404 (2017).
36. A. Okada, et al. Magnetization dynamics and its scattering mechanism in thin CoFeB films with interfacial anisotropy. *Proc. Natl. Acad. Sci. USA* **114**, 3815 (2017).
37. K. Zakeri, et al. Spin dynamics in ferromagnets: Gilbert damping and two-magnon scattering. *Phys. Rev. B* **76**, 104416 (2007).
38. G. Woltersdorf, and B. Heinrich, Two-magnon scattering in a self-assembled nanoscale network of misfit dislocations. *Phys. Rev. B* **69**, 184417 (2004).
39. R. Arias and D. L. Mills, Extrinsic contributions to the ferromagnetic resonance response of ultrathin films, *Phys. Rev. B.* **60**, 7395 (1999).
40. Z. Chen, W. Kong, K. Mi, G. Chen, P. Zhang, X. Fan, C. Gao and D. Xue, The anisotropic effective damping of thickness dependent epitaxial Co2FeAl films studied by spin rectification, *Appl. Phys. Lett.* **112**, 122406 (2018).
41. M. Beleguenai et al., Co2FeAl thin films grown on MgO substrates: Correlation between static, dynamic, and structural properties, *Phys. Rev. B.* **87**, 184431 (2013).
42. M.B. Jungfleisch et al., Insulating Nanomagnets Driven by Spin Torque. *Nano Letters*, **17**, 1 (2017).
43. Y. Cheng et al., Nonlocal Uniform-Mode Ferromagnetic Resonance Spin Pumping. *Nano Letters*, **20**, 10, 7257, (2020).
44. D.L. Mills, and S.M. Rezende, *Spin Dynamics in Confined Magnetic Structures II*, edited B. Hillebrands and K. Ounadjela (Springer-Verlag, Berlin, 2003).

45. A.A. Serga, A.V. Chumak, and B. Hillebrands, YIG magnonics. *J. Phys. D: Appl. Phys.* **43**, 264002 (2010).
46. A.V. Chumak, V.I. Vasyuchka, A.A. Serga, and B. Hillebrands, Magnon spintronics. *Nat. Phys.* **11**, 453-461 (2015).
47. A.V. Chumak, A.A. Serga, and B. Hillebrands, Magnonic crystals for data processing. *J. Phys. D: Appl. Phys.* **50**, 244001 (2017).

Supplementary information

Facet controlled anisotropic magnons in $Y_3Fe_5O_{12}$ thin films

Rohit Medwal[#1], Angshuman Deka[#2†], Joseph Vimal Vas[1], Martial Duchamp[3], Hironori Asada[4], Surbhi Gupta[1,2], Yasuhiro Fukuma[2,5*], and Rajdeep Singh Rawat[1*]*

[1]Natural Sciences and Science Education, National Institute of Education, Nanyang, Technological University, Singapore 637616 Singapore

[2]Department of Physics and Information Technology, Kyushu Institute of Technology, Iizuka 820-8502, Japan

[3]Laboratory of In-situ and Operando Electron Nanoscopy (LISION), School of Material Science and Engineering, Nanyang Technological University, Singapore 637616 Singapore

[4]Graduate School of Sciences and Technology for Innovation, Yamaguchi University, Ube 755-8611, Japan

[5]Research Center for Neuromorphic AI hardware, Kyushu Institute of Technology, Kitakyushu 808-0196, Japan

[#]These authors contributed equally

Correspondence* rajdeep.rawat@nie.edu.sg,

Co-correspondence** surbhi.gupta@nie.edu.sg, fukuma@cse.kyutech.ac.jp

†*Current affiliation:* Purdue University, School of Electrical and Computer Engineering, Birck Nanotechnology Center, West Lafayette, Indiana 47907, USA.

S1. Deposition and characterization techniques

Prior to deposition, GGG substates with different facets i.e. GGG (001), GGG (011) and GGG (111) were cleaned using ethanol in ultrasonic bath for 5 minutes and then dried with nitrogen flow and placed in the sputtering chamber. The deposition was carried out at 100 W rf power in the presence of partial oxygen pressure of 1 Pa to maintain the oxygen stoichiometry of YIG thin films. The deposited YIG thin films were then annealed at 750 °C for 4 hours with the ramp rate of 8 °C/minute under the ambient atmospheric conditions, followed by cooling down to 400 °C at a rate of 1 °C/minute. Thereafter, the samples were cooled down to room temperature without controlling the cooling rate. It was a natural cooling in the ambient atmosphere. It is important to highlight that all YIG thin films on the GGG substrates of different orientations are deposited and annealed at same time to avoid any mismatch processing conditions. To examine the crystallographic properties of deposited YIG thin films, symmetric and asymmetric X-ray diffraction (XRD) measurements were performed using Bruker D8 Discover. The magnetic properties of the thin films were estimated by broadband FMR measurement set-up using a vector network analyzer (VNA, Model: Agilent N5222A). In this method, 2×2 mm^2 pieces of YIG thin film samples grown on a GGG substrate with different orientations, is placed on a coplanar waveguide (CPW), that has a 50 μm wide signal line, with the substrate facing away from the CPW. Microwave signal of fixed frequency f is applied to the CPW. The direction of the microwave current I_{rf} flowing in the CPW sets up an in-plane hrf acting on the magnetic layer. The reflection coefficient S11 spectra were recorded using the VNA at fixed f by the varying in-plane static magnetic field Hex.

S2. Crystallographic studies

The XRD measurements were performed in locked coupled mode to investigate the epitaxy of the thin film. For YIG (001)/GGG (001), two distinct peaks corresponding to YIG (004)/GGG (004) and YIG (008)/GGG (008) were observed as shown in Figure 1(a). Further, high resolution (2θ–ω) XRD scans of YIG (001) reveals the presence of YIG (004) at 28.63° and YIG (008) at 59.43°, together with resolved $K\alpha_1$ and $K\alpha_2$ peaks of GGG (004) and GGG (008) as shown in the Figure 1(b). The YIG grown on the GGG (011) and GGG (111) also shows the *hkl* reflections corresponding to (011) (Figure 1 (c) and (d)) and (111) (Figure 1 (e) and (f)), respectively. This confirms the formation of single phase epitaxial YIG thin film as per the orientation of GGG substrates.

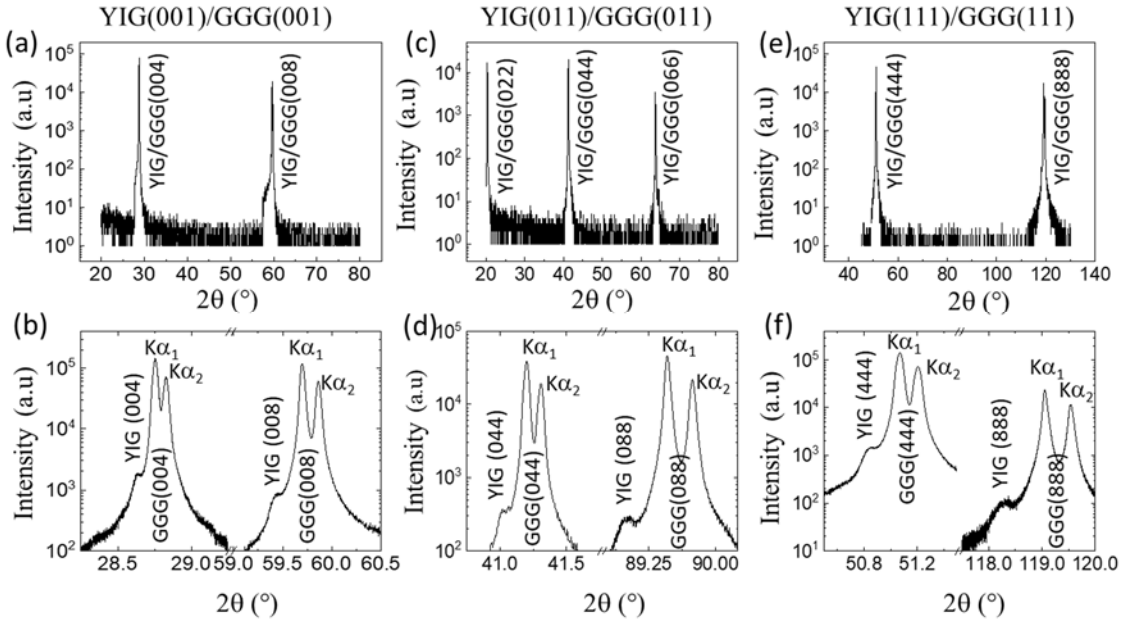

Fig 1. Symmetric XRD pattern for **(a)** YIG (001)/GGG (001) sample showing the Bragg reflections corresponding to (004) and (008) planes. **(b)** High resolution 2θ– ω for YIG (001)/GGG (001). **(c)** Symmetric XRD pattern and **(d)** High resolution 2θ– ω of YIG (011)/GGG (011). **(e)** Symmetric XRD pattern and **(f)** High resolution 2θ– ω of YIG (111)/GGG (111).

To further support the epitaxial growth of the deposited YIG thin film and identify the in-plane crystallographic directions, out of plane asymmetric XRD scans were performed. The

Bragg reflection (888) was accessed for YIG (001) and YIG (011) thin film using high resolution (2θ–ω) XRD scan, as shown in Figure 2(a)-(b). The presence of (888) reflection at 2θ=118.21° (for YIG (001, refer Figure 2 (a)) and 2θ= 118.22° (for YIG (011, refer Figure 2 (b)) matches well with the symmetric (888) plane of YIG (111) centred at 2θ=118.21° (refer Figure 1 (f)). Similarly, asymmetric XRD scan for Bragg reflection (088) for YIG (111) is observed at 2θ=88.99° as shown in Figure 2(c), which also matches well with symmetric scan of (088) of YIG (011) cantered at 2θ=88.99° shown in Figure 1(d). Thus, XRD measurement confirm the deposition of single phase epitaxial YIG (001), YIG (011) and YIG (111) thin film on their respectively GGG substates. Further, to mark the in-plane stereographic projections in the YIG (001)/GGG (001), YIG (011)/GGG (011) and YIG (111)/GGG (111), asymmetric XRD scans were recorded as function of in-plane angle from 0° to 360°. The in-plane projection of the (888) plane in the YIG (001) shown in Figure 2(d) would result in the in-plane [011] direction. However, projection of YIG (888) in YIG (011) thin film shown in Figure 2(e) would result in in-plane [001] direction. The angle dependent asymmetric scan of YIG (088) for YIG (111) thin film results in three-fold symmetry as shown in Figure 2(f). The projection of asymmetric scan of (088) result in the in-plane $[11\bar{2}]$ direction.

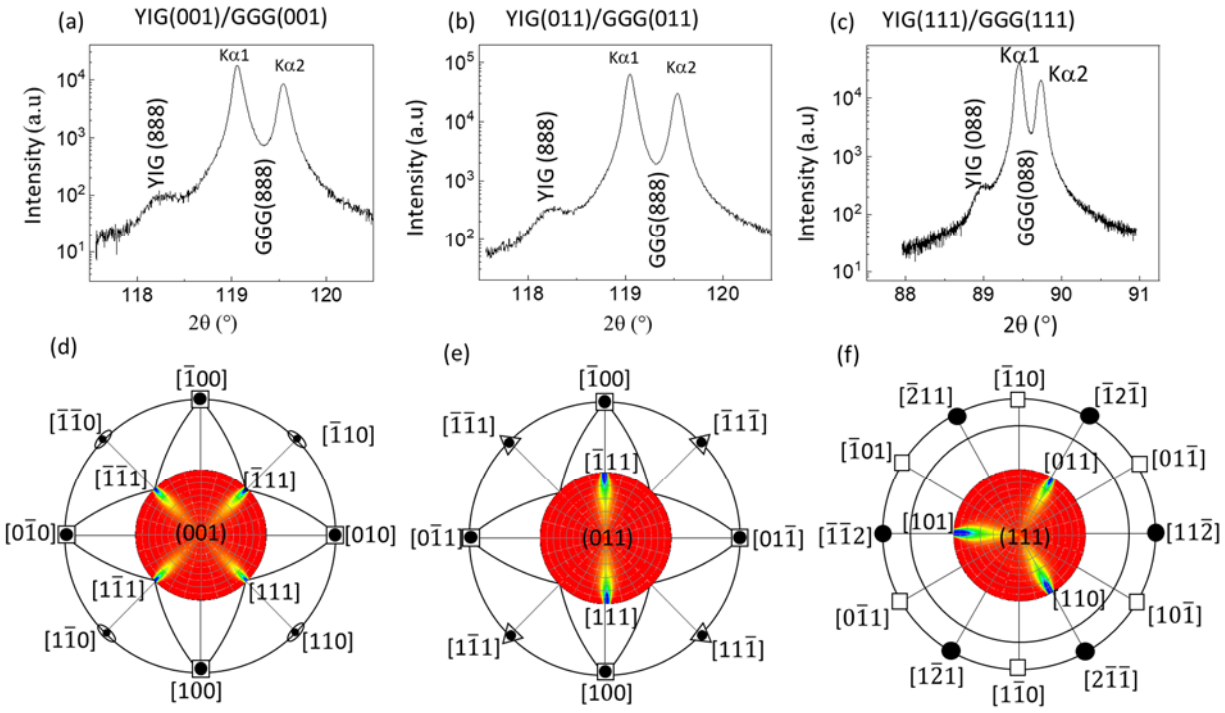

Fig 2. Asymmetric 2θ–ω XRD pattern (a) YIG (001)/GGG (001), (b) YIG (011)/GGG (011) and (c) YIG (111)/GGG (111). Asymmetric phi scan for (d) (888) Bragg reflection of YIG (001)/GGG (001), (e) (888) Bragg reflection of YIG (011)/GGG (011) and (f) (088) Bragg reflection of YIG (111)/GGG (111).

S3. Cross-sectional TEM sample preparation

The epitaxial growth of the films is characterized by atomically resolved high-angle annular-dark-filed (HAADF) scanning transmission electron microscopy (STEM) measurements performed in double corrected JEOL Grand ARM300 equipped with cold FEG gun at 300 kV. The cross-sectional samples required for the TEM characterization were prepared using a Zeiss Crossbeam 540 FIB equipped with dual gun and an in-situ micromanipulator for transferring the cross-section sample to the TEM half-grid as shown in Figure 3 (a). In-order to protect the sample from damage due to the ion beam, 2 Pt layers were deposited sequentially -first with the electron beam and then the ion beam. The cross-sectional samples were prepared and thinned down to electron transparency as shown in the Figure 3 (b). The milling current was

reduced from 30 kV, 700 pA to 50 pA until the thickness of the lamella was ~ 600 nm. The milling was then done at 5 kV and 10 pA to minimize gallium implantation.

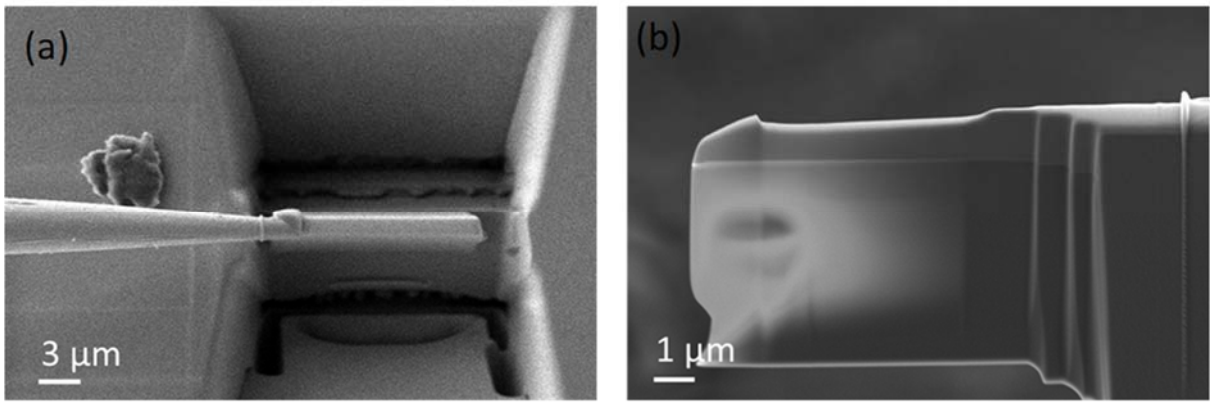

Figure 3. Sample preparation using focused ion beam (a) lamella lift off (using omni probe) from trench created in FIB and (b) lamella attached to TEM half grid, thinned down to electron transparency.

S4. Power dependent resonant field and linewidth

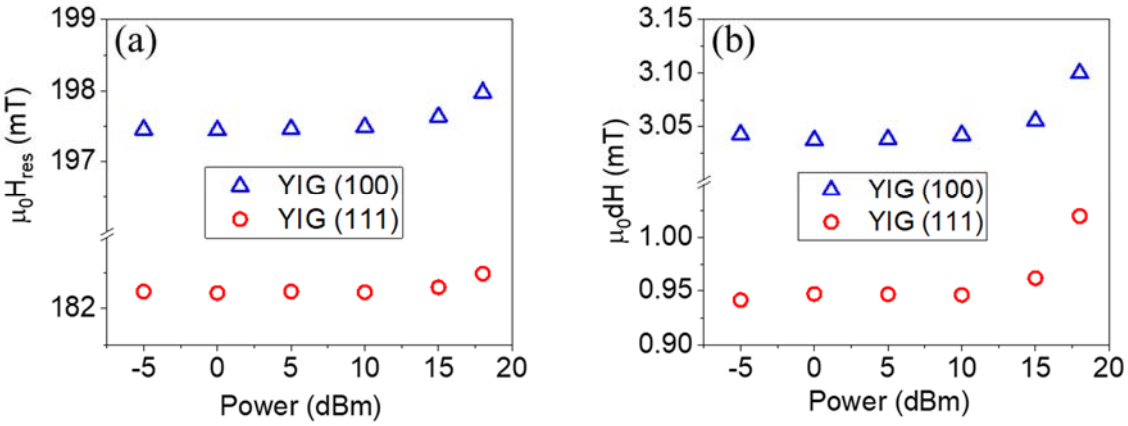

Figure 4: Resonant field and linewidth of (a) YIG (100) and (b) YIG (111) as a function of excitation power.

S5. Schematic showing the origin of anisotropy

This growth induced magneto-crystalline anisotropy (MCA) can be explained using the framework of short-range ordering of the Fe^{3+} cation pairs in the garnet film during the crystalline growth. Two types of relevant rare earth Fe^{3+} pair ordering- tetrahedral and

octahedral, are present in the film as shown in Figure 4(a), which arises from the bonding between Fe^{3+} and O^{2-}. The arrangement of the tetrahedral and octahedral sublattices in the YIG lattice for the three kinds of epitaxial growths are shown in Figure 4(b)-(d). While the ordering of both tetrahedral and octahedral sublattices in YIG (001) show a cubic symmetry, only the tetrahedral ordering in YIG (011) has a cubic arrangement with the octahedral showing a uniaxial symmetry.

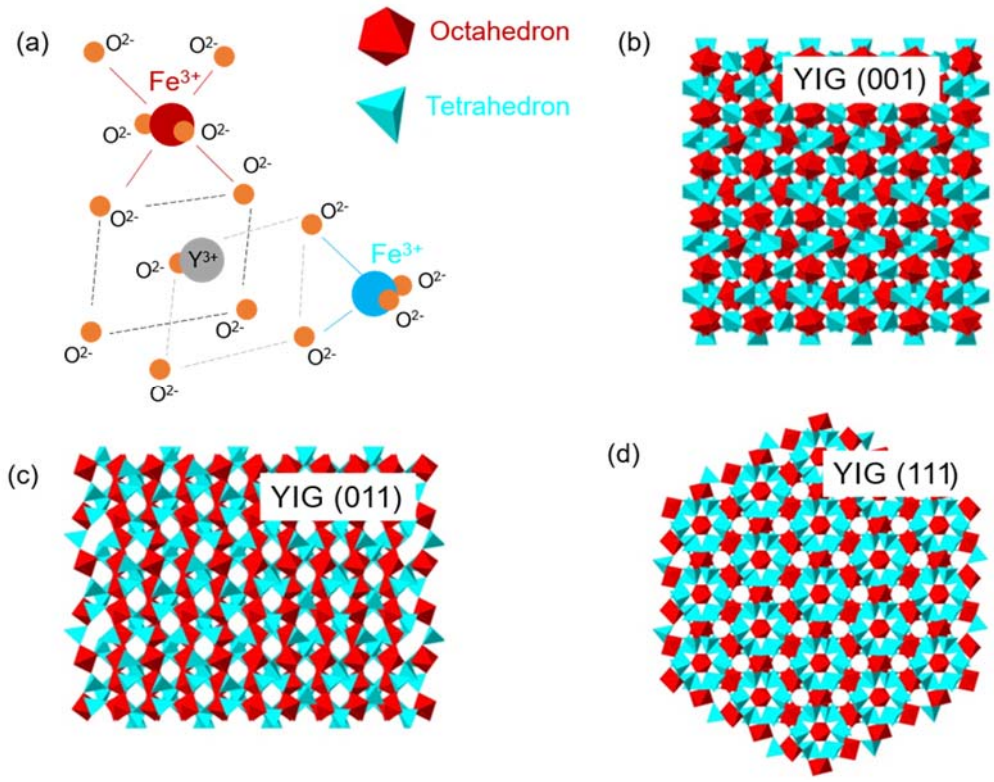

Figure 5. (a) Schematic of the octahedral and tetrahedral sublattices of a YIG crystal lattice showing the arrangement of Y^{3+}, Fe^{3+} and O^{2-} ions. Arrangement of the sublattices in YIG **(b)** (001) **(c)** (011) and **(d)** (111). Octahedrons are denoted by red while the tetrahedral sublattices are depicted by blue.